Bubble Driven Quasioscillatory Translational Motion of Catalytic Micromotors

Manoj Manjare, Bo Yang, and Y.-P. Zhao

Phys. Rev. Lett. **109**, 128305 — Published 21 September 2012

DOI: 10.1103/PhysRevLett.109.128305

Bubble driven quasi-oscillatory translational motion of catalytic micromotors

Manoj Manjare, [1] Bo Yang, [2] and Y.-P. Zhao[1]

[1]Nanoscale Science and Engineering Center

Department of Physics and Astronomy

The University of Georgia, Athens, GA 30602

[2]Department of Mechanical and Aerospace Engineering

University of Texas, Arlington 76019

Abstract

A new quasi-oscillatory translational motion has been observed for big Janus catalytic micromotors with a fast CCD camera. Such motional behavior is found to coincide with both the bubble growth and burst processes resulting from the catalytic reaction, and the competition of the two processes generates a net forward motion. Detailed physical models have been proposed to describe the above processes. It is suggested that the bubble growth process imposes a growth force moving the micromotor forward while the burst process induces an instantaneous local pressure depression pulling the micromotor backward. The theoretic predictions are consistent with the experimental data.

PACS Number: 82.70.Dd, 83.10.Pp, 47.55.dd, 45.50.Dd

Microstructures moving in low Reynolds number environments have been extensively studied recently [1, 2]. Numerous groups have focused on catalytic nanomotors [3-7] , which utilize a catalyst to derive energy from the surroundings. For these studies, the two most common fuels used are H_2O_2 [5, 8, 9] and glucose [10]. A nano-/micro- structure with a catalyst asymmetrically coated on the surface, converts chemical energy directly into kinetic energy through the reaction $H_2O_2 \rightarrow H_2O+O_2$ [2, 7, 10-13]. The exact propulsion mechanisms by which these motors move depends on their structure and composition. For metal-catalyst heterojunction structures, the nanomotor was observed to move toward the direction of the catalyst/solution interface, and the propulsion mechanism has been explained by the interfacial tension gradients [8] or self-electrophoresis mechanism [14]. For insulator-catalyst hetero-structures, the nanomotor was observed moving away from the catalytic/solution interface, and bubble propulsion [6, 9, 15], self-electrophoresis osmotic pressure [16], and diffusiophoresis [17] have all been proposed to explain the motion mechanism. In particular, previous theoretical treatments of bubble propulsion [9] suggest that the bubbles leave the catalyst surface, impart a net momentum on the surface, and drive the motors. However, previous studies of spherical nanomotors, i.e. Janus particles, have not directly confirmed such a phenomenon. Only very recently rolled-up tubular microjets have been observed to eject bubbles from one end, acting as thrusters, with a maximum translational speed of 10 mms^{-1} [18-20]. However, the tubular structure has a very different mass transport and bubble formation mechanism than the spherical micromotor since the catalyst is inside the tubular structure, and the detailed geometry of the tubes such as the symmetry of the tube, the size and shape of tube openings, and the tube length, controls the H_2O_2 fuel supplying process. According to Fletcher [21], the large curvatures of previously studied spherical nanomotors resulted in large bubble formation energies, which made it difficult for bubbles to nucleate, grow, and detach from the catalytic surface. Therefore, in order to allow the bubbles to grow and form on a catalytic surface, the motor must possess a smaller curvature.

We have performed a systematic study on the kinematic behavior of spherical catalytic micromotors with different diameters, 2 μm, 3 μm, 5 μm, and a distribution of beads between 10-50 μm, to investigate the size dependent propulsion mechanism by fixing the H_2O_2 concentration (5%). The bubbles begin to appear on the micromotors when the diameter of the beads is larger than 10 μm. With increasing bead size, the bubbling occurs more readily, which is consistent with Fletcher's prediction [21]. Surprisingly, the motion kinematics of these larger motors are very different from those of previously reported small motors; the trajectory follows a quasi-oscillatory pattern rather than a linear motion. Such a process demonstrates a novel propulsion mechanism for catalytic micromotors. With a fast CCD camera, a systematic study has revealed that the motion of the micromotor coincides with the bubble growth/disappearance process: when the bubble grows and evolves on the catalytic surface, the motor moves away from the center of the bubble due to the bubble growth force; once the bubble reaches a maximum radius, it suddenly disappears (within 50 μs). Such a sudden disappearance, referred to as a bubble burst process, generates a local pressure depression that pulls the bead back towards the bubble location, and imparts a large impulse on the bead. Although the motion due to bubble bursting on a larger scale has been observed [22], this rocking motion induced by the bubble growth/burst has not been observed and understood before, to the best of our knowledge.

Silica beads with mean diameters of 10 - 50 μm are uniformly spread on a Si substrate with the help of a double-sided tape. An ~10 nm adhesion layer of Ti is deposited on these beads in an electron beam evaporation system at a growth rate of 0.05 nm/s (measured by a quartz crystal microbalance), then a layer of Pt with a thickness of ~ 25 nm is deposited at 0.05 nm/s, as shown in Fig. 1(a). After the deposition, the substrates with coated beads are soaked in Hexane for about 20 minutes. This separates the beads from the tape with the help of tweezers. Most of the hexane is then pipetted out after centrifuging the mixture at 3000 rpm, leaving the beads at the bottom of a vial. Then Toluene is introduced to the vial in order to remove hexane and any leftover of tape glue residue on the beads. The mixture is again centrifuged. This process is repeated three times to ensure that the hexane is completely replaced by Toluene. To replace Toluene with water, the mixture has to go through intermediate steps of re-suspensions. After centrifuging the mixture, Toluene is replaced by Isopropanol followed by Ethanol and then water. Finally, the beads are suspended in 18 MΩ de-ionized (DI) water. Fig. 1(b) shows a scanning electron microscope (SEM) image of one such bead. A droplet (5 μl) containing a few beads is then observed under the microscope, 10% peroxide (5 μl) is then added to the droplet. Isolated single beads are randomly selected in order to observe independent motion. The motion of the beads is recorded at 1000, 5000, and 20,000 fps with a CCD camera (Phantom v9.1) using 10× magnification objective lens of a Mitituya FS110 microscope.

Figure 1(c) shows the representative snapshots at every 0.01 s for one complete cycle of bubble growth/burst process extracted from one video [23]. The $t = 0$ s frame shows a bead of diameter ~ 45 μm and an attached maximally sized bubble with a diameter of 73 ± 2 μm. At $t = 0.01$ s, the big bubble disappears (burst), and multiple small bubbles start to grow on one side of the bead (catalytic surface), and some small bubbles coalesce and become a big bubble. Such a big bubble does occasionally detach from the bead, as shown in the frame $t = 0.02$ s, and then re-attach back to the bead ($t = 0.03$ s). The big bubble continues to grow at the expense of small bubbles due to the Ostwald ripening effect ($t = 0.04$ s to 0.07 s) [24], until it reaches a maximum size (t = 0.08 s). The bubble bursts (t = 0.09 s), and the entire process repeats. The entire repeated process takes about 0.06 – 0.12 s. During the big bubble growth, the center of the big bubble displaces towards the bead slightly (~ 3 to 7 μm) after the bubble reattachement, while the bead is pushed to a distance ~ 30 μm away from the bubble (toward the up-right direction in Fig. 1(c)). When the bubble bursts (from t = 0 s to 0.01 s, or from t = 0.08 s to 0.09 s), the center of the bead moves toward the center of the previous bubble (to the lower-left direction in Fig. 1(c)). Figure 1(d) shows the trajectory of the center of the bead after four such bubble growth/burst cycles. It demonstrates a quasi-oscillatory translational motion behavior: the bubble growth process pushes the bead forward while the bubble burst process pulls the bead back. However, the growth process produces a larger overall displacement compared to that of the burst process; therefore, there is a net displacement of the bead in the forward direction.

The dynamics of the bead motion during the bubble growth/burst process were studied in detail by 20,000 fps videos. By careful examination of the high speed video, we find that the bubble burst induced bead motion is accompanied by small timescale wave generation due to bubble collapse. Figure 2(a) shows four consecutive images taken at/after the burst of the bubble. With respect to the first image, at t = 50 μs, a wave pattern is generated around the bubble-bead system; at t = 100 μs, the bubble is gone and a propagating wave front is observed. At t = 150 μs, the wave pattern disappears, indicating the short life of the bubble burst event. The bubble burst and the generation of the wave pattern are the result of bubble shrinkage due to mass transport of O_2 at the gas-liquid boundary. The bubble growth/shrinkage is governed by the Rayleigh-Plesset equation [25],

$$P_b = P_\infty + \frac{2\sigma}{R} + \frac{4\eta}{R}\dot{R} + \rho\left(R\ddot{R} + \frac{3}{2}\dot{R}^2\right), \tag{1}$$

where P_b, P_∞, R, σ, and ρ are the pressure of gas inside the bubble, the pressure of the liquid at remote distances (≈ 101 kPa, the atmospheric pressure), the radius of the bubble, the surface tension, and the mass density of water, respectively. Assuming that the gas inside the bubble follows the ideal gas equation, $P_b V_b = n_b R_g T$, where n_b is the mole number of gas molecules, R_g is the gas constant, and T is the temperature. At the moment of the burst, the O_2 flux flowing into the bubble supplied by the catalytic reaction is smaller than the flux leaking from the bubble to the liquid. At the boundary of the bubble, the net O_2 flux from the bubble into the water α is assumed to be a constant,

$$\dot{n}_b = -\alpha A_b, \tag{2}$$

where $A_b = 4\pi R^2$ and $V_b = 4\pi R^3/3$. The fluid pressure at the bubble boundary, $P_l = P_b - 2\sigma/R$, determines how the bead would move. By solving Eqs. (1) and (2) numerically, the time dependent normalized $R(t)/R(0)$ and P_l/P_∞ for $\alpha = 10$, 30 and 50 moles/(s·m^2) (*From the shrinking of the bubble, experimentally* α *can be estimated as* $\alpha \approx 24$ *moles/(s·m*^{2}*)*) are plotted in Fig. 2(b). For $\alpha \geq 30$ moles/(s·m^2), the bubble shrinks to zero in 50 μs. Such a shrinkage is accompanied with temporal oscillations of R and P_l. These oscillations could explain the observed wave pattern. When $P_l/P_\infty < 1$, a pressure depression region appears around the bubble, and liquid will flow inbound; when $P_l/P_\infty > 1$, the high P_l will push the liquid out of the bubble region. However, Fig. 2(b) shows that within 50 μs (time interval between two consecutive video frames), the $P_l/P_\infty < 1$ region is greater than $P_l/P_\infty > 1$ region, giving an effective depression. It indicates that the bead is pulled back towards the bubble location during the burst process.

The back-pull on the micromotor due the bubble burst produces negative displacement. Figure 3(a) shows the instantaneous velocity $v(t)$ of the bead as a function of time t extracted from three burst events. The negative sign indicates that the velocity is against the net displacement. After the bubble burst, the initial speed of the bead can reach as high as 14 cm/s, which corresponds to a speed to body length ratio of 1,000. Such an initial speed imparts an effective impulse of $I = 1.26 \times 10^{-11}$ Ns, or a pressure of 1.3 Torr on the bead, at the moment of bubble burst. Additionally, the Reynolds number jumps instantaneously to ~ 3, then falls to ~ 10^{-2} within 0.1 ms. With the small Reynolds number, the motion of the bead is governed only by the drag force, F_{drag}, which results from the viscosity effect and potential wall effect due to proximity to the substrate stage [26], $F = -F_{drag}$, where

$$F_{drag} = 6\pi\eta R_m v\left(1+\frac{R_m}{\sqrt{\pi\upsilon t}}+\frac{9}{16}\frac{R_m}{\lambda}\left(\frac{\upsilon t}{3\lambda^2}\right)\right), \tag{3}$$

for a spherical bead of radius R_m and mass m moving with a velocity v at a vertical distance (from the center of the bead) λ to the wall, in a fluid with viscosity η, density ρ, and kinematic viscosity υ. The velocity of the bead v can be expressed as,

$$v = v_0 e^{-k\left(At^{1/2}+t+Bt^2\right)}, \tag{4}$$

where $A = \frac{2R_m}{\sqrt{\pi\upsilon}}$, $B = \frac{9}{32}\frac{R_m}{\lambda}\left(\frac{\upsilon}{3\lambda^2}\right)$, and $k = 6\pi\eta R_m / m$. By fitting the experimental data in Fig. 3(a) using Eq. (4), as shown in the dashed curves, one obtain $\eta = 0.0011 \pm 0.0002$ Ns/m^2 and $\lambda = 40 \pm 3$ μm, i.e., the viscosity is approximately the value of water, while λ is close to the radius of the maximum bubble (diameter ~ 73 ± 2 μm). This implies a possibility that the bubble is lifting the bead during the bubble growth, and the bead is moving horizontally on top and close to the observation substrate.

After the large bubble bursts, small bubbles start to nucleate and grow on the catalytic surface again as shown in Fig. 1(c), and the velocity of the bead instantaneously reaches a high positive value (~ 0.4 – 1.2 cm/s) as shown in Fig. 3(b), and then decreases quickly within 10 ms. This behavior is closely associated with bubble growth. Figure 4 plots the measured radius $R(t)$ of the big bubble and relative distance $S(t)$ travelled by the bead versus time t for three separate cycles. Interestingly, the S–t relationship follows the pattern of $R(t)$, which suggests that the movement of the bead is closely related to the advancing of the bubble boundary. According to Thorncroft et al [27], during the bubble growth, the R–t relation can be approximated by a power law, $R = \gamma t^n$, where n is the growth exponent and γ is the proportionality constant. If the rate of O_2 flow, Q, into the (major) bubble (at the expense of surrounding small bubbles *via* Ostwald ripening) is assumed to be a constant, then for the bubble volume, $V = Qt$. Thus, for a spherical bubble one should expect $n = 0.33$. Indeed, the big bubble on the catalyst surface follows above power law, with $n = 0.36 \pm 0.01$ (see Fig. 4). The corresponding $S - t$ curves also follow similar power law (Fig. 4).

The driving mechanism for the bead during the bubble growth process is the result of two opposite forces,

$$F = F_{growth} - F_{drag} . \tag{5}$$

The growth force F_{growth} is due to bubble growth [28], $F_{growth} = \pi \rho R^2 \left(\frac{3}{2} C_s \dot{R}^2 + R\ddot{R} \right)$, where C_s is an empirical constant that modifies the growth force, and the drag force, $F_{drag} = 6\pi\eta R_m v$, is due to the motion of the bead as shown in the inset of Fig. 3(b). Considering the power law behavior of bubble growth, the velocity of the bead can be expressed as,

$$v = \left(\beta \int_0^t t^{4n-2} e^{kt} \, dt \right) e^{-kt} , \tag{6}$$

where $\beta = \gamma^2 \frac{\rho\pi}{m}\left[\frac{3}{2}C_s(\gamma n)^2 + \gamma^2 n(n-1)\right]$. By solving Eq. (6) numerically we can obtain the fitting for bead velocity $v(t)$ as shown in Fig. 3(b) with C_s = 900 ± 140. The outliers shown in Fig. 3(b) are instances when random coalescing between bubbles occurs and when the bubble detaches and re-attaches to the bead (See Fig. 1(c) for t = 0.02 s). Equation (6) describes the bead motion very well for the bubble growth process. In the meantime, the bubble grows steadily and moves slowly with low Reynolds number (~ 10^{-7}). Using Stokes law, $F_{growth} = F_{drag}^{b}$, and $R = \gamma t^n$ with $F_{drag}^{b} = 6\pi\eta R v_b$, we obtain the velocity of the bubble $v_b = Et^{-1}$ with $E = \frac{\gamma^3}{6\upsilon}\left(\frac{1}{6}C_s - \frac{2}{9}\right) = (9 \pm 3)\mu\text{m}$. The bubble displacement is expressed as $S_b = E\ln(t/t_0)$ with the bubble reattachment time $t_0 \approx 0.04$s. This equation can be used to fit the experimental data as shown in Fig. 4, and the best fit gives $E \approx 6$ µm, which is consistent with the above prediction.

In conclusion, we have observed new quasi-oscillatory translational motion dynamics of big Janus micromotors. The observed motional behavior is due to bubble growth and burst processes occurring during the catalytic reaction. The competition between these two processes creates a different and complicated driving mechanism for catalytic micromotors: the bubble growth process imposes a growth force to move the micromotor forward while the burst process induces an instantaneous local pressure depression to pull the micromotor backward. The physical origins for this motion have been identified and the proposed models fit the experimental data very well. It is expected that these models could be used to describe other bubble propelled micro/nanomotors.

We thank George Larsen for proof-reading this manuscript. This research was funded by National Science Foundation under contract No. ECCS-0901141.

References

[1] G. A. Ozin, I. Manners, S. Fournier-Bidoz, A. Arsenault, Adv Mater **17**, 3011 (2005).

[2] W. F. Paxton, S. Sundararajan, T. E. Mallouk, A. Sen, Angew Chem Int Edit **45**, 5420 (2006).

[3] T. Mirkovic, N. S. Zacharia, G. D. Scholes, G. A. Ozin, Acs Nano **4**, 1782 (2010).

[4] J. Wang, and K. M. Manesh, Small **6**, 338 (2010).

[5] J. Gibbs, and Y. Zhao, Frontiers of Materials Science **5**, 25 (2011).

[6] Y. F. Mei, A. A. Solovev, S. Sanchez, O. G. Schmidt, Chem Soc Rev **40**, 2109 (2011).

[7] Y. Y. Hong, D. Velegol, N. Chaturvedi, A. Sen, Phys Chem Chem Phys **12**, 1423 (2010).

[8] W. F. Paxton, K. C. Kistler, C. C. Olmeda, A. Sen, S. K. St Angelo, Y. Y. Cao, T. E. Mallouk, P. E. Lammert, V. H. Crespi, J Am Chem Soc **126**, 13424 (2004).

[9] J. G. Gibbs, and Y. P. Zhao, Appl Phys Lett **94**, 163104 (2009).

[10] N. Mano, and A. Heller, J Am Chem Soc **127**, 11574 (2005).

[11] Y. P. He, J. S. Wu, Y. P. Zhao, Nano Lett **7**, 1369 (2007).

[12] D. Kagan, S. Campuzano, S. Balasubramanian, F. Kuralay, G. U. Flechsig, J. Wang, Nano Lett **11**, 2083 (2011).

[13] S. Sanchez, A. A. Solovev, Y. F. Mei, O. G. Schmidt, J Am Chem Soc **132**, 13144 (2010).

[14] Y. Wang, R. M. Hernandez, D. J. Bartlett, J. M. Bingham, T. R. Kline, A. Sen, T. E. Mallouk, Langmuir **22**, 10451 (2006).

[15] T. Mirkovic, N. S. Zacharia, G. D. Scholes, G. A. Ozin, Small **6**, 159 (2010).

[16] U. M. Cordova-Figueroa, and J. F. Brady, Phys Rev Lett **100**, 158303 (2008).

[17] R. Golestanian, T. B. Liverpool, A. Ajdari, Phys Rev Lett **94**, 220801 (2005).

[18] Y. F. Mei *et al.*, Adv Mater **20**, 4085 (2008).

[19] K. M. Manesh, M. Cardona, R. Yuan, M. Clark, D. Kagan, S. Balasubramanian, J. Wang, Acs Nano **4**, 1799 (2010).

[20] S. Sanchez, A. N. Ananth, V. M. Fomin, M. Viehrig, O. G. Schmidt, J Am Chem Soc **133**, 14860 (2011).

[21] N. H. Fletcher, J Chem Phys **29**, 572 (1958).

[22] R. F. Ismagilov, A. Schwartz, N. Bowden, G. M. Whitesides, Angew Chem Int Edit **41**, 652 (2002).

[23] See Supplemental Material at [URL will be inserted by publisher]. The video "bubble_movie_1" shows the motion of a micromotor captured at 20,000 fps and played at 25 fps. Similar motions have been observed for many other motors. Movies "bubble_movie_2" and "bubble_movie_3" are two other examples captured at 5,000 fps and played at 25 fps.

[24] P. W. Voorhees, Annu Rev Mater Sci **22**, 197 (1992).

[25] J.-P. Franc, and J.-M. Michel, *Fundamentals of cavitation* (Kluwer Academic Publishers, Boston, 2004).

[26] J. Happel, *Low Reynolds number hydrodynamics With special applications to particulate media* (Leyden, Noordhoff International Publishing, 1973).

[27] G. E. Thorncroft, J. F. Klausner, R. Mei, Int J Heat Mass Tran **41**, 3857 (1998).

[28] L. Z. Zeng, J. F. Klausner, R. Mei, Int J Heat Mass Tran **36**, 2261 (1993).

Figure Captions

FIG. 1. (a) Schematic showing the deposition of Ti and Pt on the microbeads. (b) A SEM image of the resulting Pt-coated Silica Janus bead. (c) Snapshots of a microbead (~ 25 μm) in 5% H_2O_2 solution at approximately every 200 frames (time interval of 0.01 s) showing the bubble growth/burst processes and the bead motional behavior. (d) The trajectory of the bead extracted from a 20,000 fps video. The red arrows denote the direction of trajectories of the bead after bubble burst and the green arrows represent direction the trajectories of the bead during bubble growth.

FIG. 2. (a) Waves observed at the moment at/after the bubble bursts. (b) Numerically calculated normalized bubble radius $R(t)/R(0)$ (dashed curves) and bubble pressure $P_l(t)/P_\infty$ (solid curves) after bubble burst.

FIG. 3. Instantaneous speed $v(t)$ of the micromotors as a function of time t: (a) after bubble burst and (b) during the bubble growth. The symbols are experimental data and the curves are the fittings. The insets show the free-body diagrams of the bead-bubble system for each case.

FIG. 4. The plots of the bubble radius $R(t)$ (open symbols), the accumulative bead travelling distance $S(t)$ (solid symbols), and the accumulative bubble travelling distance $S_b(t)$ (after bubble reattaching to the bead) (cross symbols) versus time t. The symbols are experimental data for different bubble growth cycles, and the dashed curves are the fitting results.

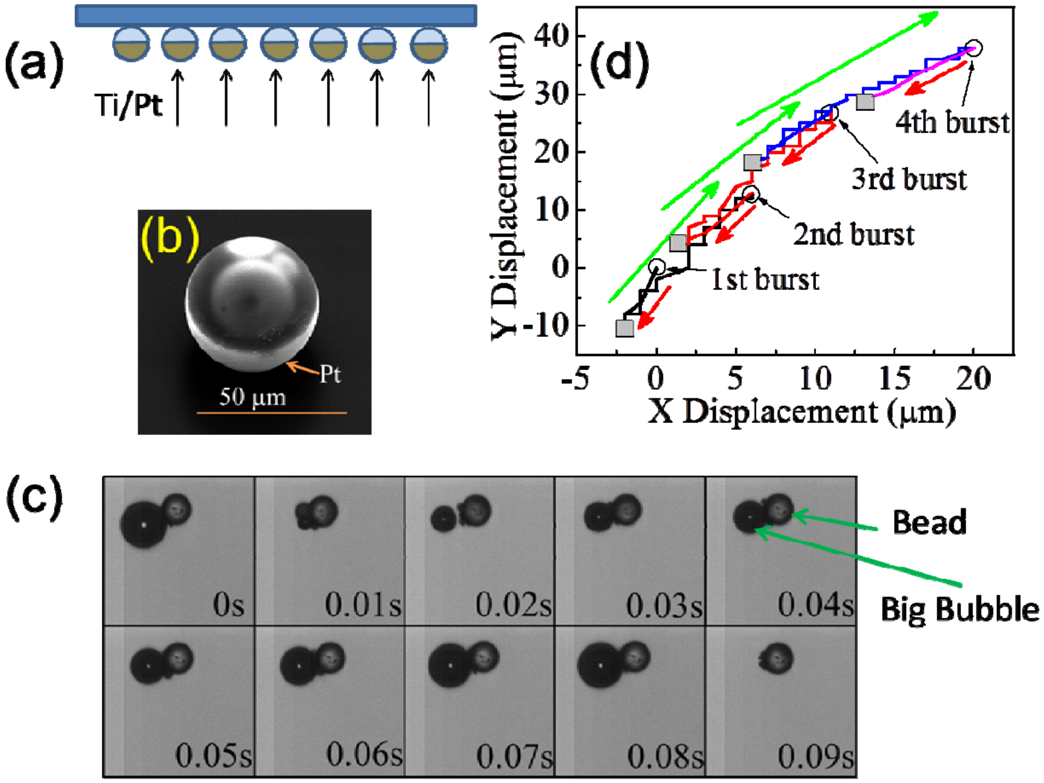

Fig. 1 Manjare et al

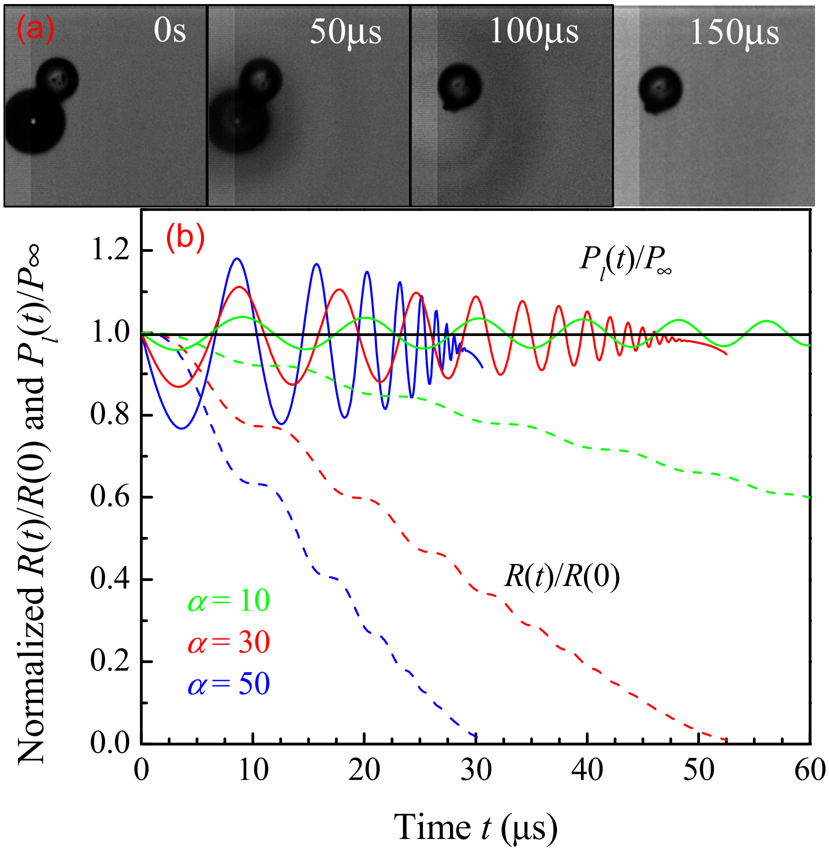

Fig. 2 Manjare et al

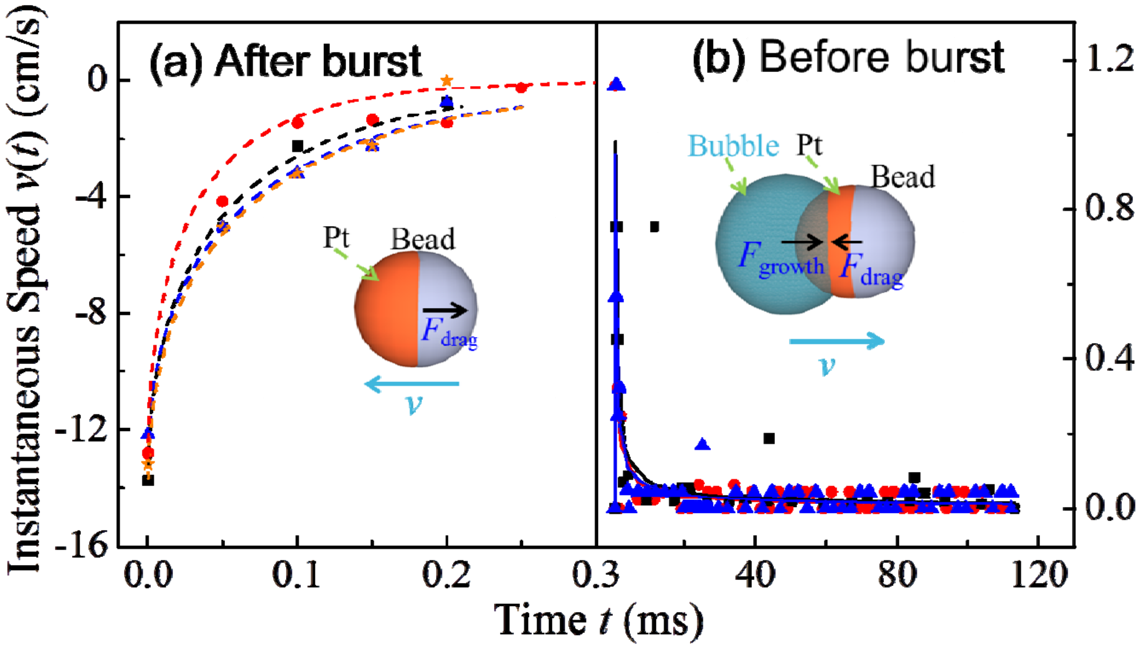

Fig. 3 Manjare et al

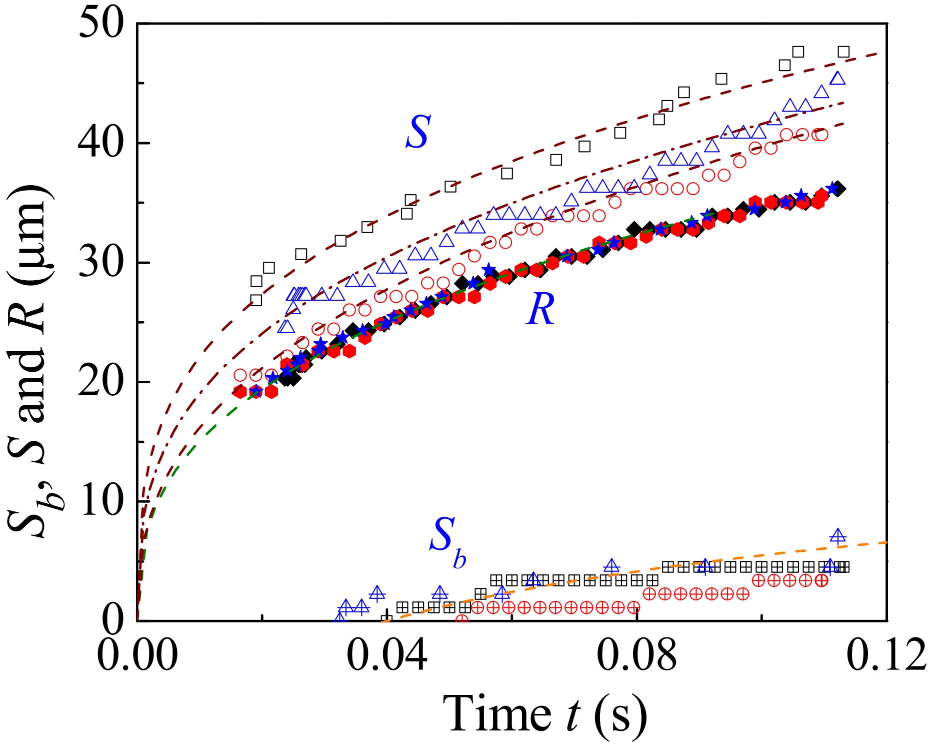

Fig. 4 Manjare et al